Carbon-doped mesoporous TiO$_2$-immobilized Ni nanoparticles: Oxygen defect engineering enhances hydrogen production

Xiaolei Zhang [a], Qilu Yao [a,*], Haochong Wu [a], Yuanlan Zhou [b], Meihua Zhu [a], Zhang-Hui Lu [a,*]

[a] *Institute of Advanced Materials (IAM), Key Laboratory of Energy Catalysis and Conversion of Nanchang, College of Chemistry and Chemical Engineering, Jiangxi Normal University, Nanchang 330022, China*
[b] *School of Mathematics and Statistics, Jiangxi Normal University, Nanchang 330022, China*

ARTICLE INFO

ABSTRACT

Constructing efficient, durable, and economical catalysts to promote hydrogen production from hydrous hydrazine (N$_2$H$_4$·H$_2$O) is crucial, but still a great challenge. Herein, noble-metal-free Cr(OH)$_3$-modified Ni nanoparticles (NPs) (2.7 nm) supported on defect-rich carbon-doped mesoporous TiO$_2$ nanosheets (C-TiO$_2$) were prepared for the first time via a simple and green wet-chemistry approach, in which the amount of oxygen defect in C-TiO$_2$ can be easily regulated by adjusting the amount of carbon doping. Significantly, the defect rich Ni-Cr (OH)$_3$/C-TiO$_2$ catalyst presented 100% H$_2$ selectivity, ultrahigh catalytic activity, and remarkable durability for N$_2$H$_4$·H$_2$O dehydrogenation, with a turnover frequency (TOF) value of 266 h^{-1} at 323 K, more than 6-fold improvement than that of the Ni-Cr(OH)$_3$/TiO$_2$ (41 h^{-1}), which is among the highest values reported so far for noble-metal-free catalysts. The superior catalytic efficiency and durability are mainly owing to the small-sized and electron-rich of Ni NPs induced by the oxygen defects in C-TiO$_2$, where the more oxygen defects, the better the catalytic activity. Furthermore, the catalyst also showed outstanding catalytic efficiency (TOF = 577 h^{-1}) and robust durability for complete dehydrogenation of hydrazine borane (N$_2$H$_4$BH$_3$) at 323 K. This work provides inspiration for the construction of defect engineering and new insights for the development of low-cost and efficient heterogeneous hydrogen production catalysts.

1. Introduction

Hydrogen is a promising renewable energy due to its extensive sources, high energy density (120 kJ/g), and environmental friendliness [1–3]. However, a safe and efficient hydrogen storage system remains one of the main technical obstacles to achieving hydrogen energy economy. In recent years, chemical storage of hydrogen has been supposed an effective method [4–10]. Among various chemical storage materials, hydrous hydrazine (N$_2$H$_4$·H$_2$O) in liquid hydrogen sources has received widespread attention due to its high hydrogen content (8.0 wt%), generation of CO-free hydrogen, convenience in storage and transport [11–15]. N$_2$H$_4$ is able to completely decompose into H$_2$ and by-product N$_2$ under appropriate catalysts and reaction conditions (Eq. (1)), while catalytic reduction of N$_2$ can regenerate N$_2$H$_4$ [16–20]. However, the decomposition of N$_2$H$_4$ can also proceed via the incomplete decomposition route (Eq. (2)) [21–23]. Therefore, developing efficient and stable catalytic materials that can complete the dehydrogenation of N$_2$H$_4$ is of great significance.

$$N_2H_4(l) \rightarrow N_2(g) + 2\,H_2(g) \tag{1}$$

$$3\,N_2H_4(l) \rightarrow 4NH_3(g) + N_2(g) \tag{2}$$

Nickel (Ni), as a non-precious metal with abundant reserves and low cost, has widely studied due to its excellent performance in various catalytic reactions as well as N$_2$H$_4$·H$_2$O dehydrogenation [24–26]. Therefore, a variety of Ni-based catalysts for N$_2$H$_4$·H$_2$O dehydrogenation have been reported so far [27–29]. Among them, Ni-based catalysts containing Pt, Rh, or other noble metals have high catalytic activity, but their application is limited due to the scarcity and high price of precious metals [30–35]. To reduce the cost of the catalysts, the development of noble-metal-free Ni catalysts is attractive [36–38]. However, there is a large gap in catalytic efficiency between non-noble metal catalysts and noble metal catalysts [39–41]. Therefore, developing a highly active noble-metal-free Ni catalyst is urgent, but still faces enormous challenges. Recent studies have shown that the catalytic activity of metal NP catalysts can be improved by doping with metal oxides or hydroxides (e.

* Corresponding authors.

E-mail addresses: yaoqilu@jxnu.edu.cn (Q. Yao), luzh@jxnu.edu.cn (Z.-H. Lu).

g. Cr(OH)$_3$) [22,24,31]. These dopants can not only act as atomic barriers to avoid active metal NP aggregating, but also act as electron donors to increase electron density of active metal surface [42]. Therefore, Cr(OH)$_3$ is expected to be as a favorable promoter of Ni catalysts to boost hydrogen production. Ultrafine active metal NPs generally showed higher catalytic efficiency due to their smaller size and thus exposure more active sites [43]. However, due to the high surface energy of metal NPs, they tend to aggregate into larger NPs, resulting in decreased activity and poor durability during the reaction. Therefore, it is highly desirable to prepare small NPs and immobilize them from aggregating by a versatile substrate.

Titanium dioxide (TiO$_2$) is one of the most popular materials in recent years because of its rich reserves, high chemical stability, and structural diversity [44–48]. In particular, mesoporous TiO$_2$ with high specific surface area and large pore size can effectively immobilize metal NPs, the number of active sites is increased and the catalytic activity is improved [49–51]. Additionally, increasing the electron density of metal active sites can also improve the catalytic activity, because it is conducive to activate the N-H bonds in N$_2$H$_4$. However, the low electron transfer efficiency at the interface of mesoporous TiO$_2$ results in insufficient electron supply around the active sites [52]. The introduction of defects in support have recently demonstrated to be an effective strategy to modulate the surface charge distribution of active sites. There are various methods for design defects, among them doping heteroatom (e. g. C, N, P) into TiO$_2$ is a popular method for constructing defects, because heteroatoms can be easily incorporated into the TiO$_2$ lattice, thereby effectively introducing oxygen vacancies (OVs) [53,54]. The OVs introduced in TiO$_2$ can induce interfacial electron transfer, increase the electron density of active metals, and strengthen the interaction between metal and support [55], thus facilitating the activation of N-H bonds in N$_2$H$_4$. Additionally, the doping of heteroatom in TiO$_2$ can also increase the specific surface area and provide a suitable coordination environment [56–58]. Therefore, the defect engineering of C-doped mesoporous TiO$_2$ may be an effective way to improve the performance of catalyst, but there are currently no reports on hydrogen production from nitrogen hydrides. At present, the incorporation of C into TiO$_2$ is usually achieved by adding carbon sources such as urea, melamine, and glucose during high-temperature calcination [59–61]. However, this method can easily lead to uneven doping and unstable defect structures, resulting in difficulty in anchoring metal NPs and low electron transfer efficiency. Therefore, developing an effective and simple strategy to engineer the defects of mesoporous TiO$_2$ for preparing small non-noble metal NPs to improve catalytic dehydrogenation activity remains challenging.

In this work, we report for the first time the immobilization of Cr (OH)$_3$-modified Ni NPs on defect-rich C-doped mesoporous TiO$_2$ via a simple and green wet-chemistry approach, where C-TiO$_2$ was synthesized using solvent-induced hydrothermal method combined with high temperature calcination. The amount of oxygen defects in C-TiO$_2$ can be regulated by simply adjusting the carbon doping amount, which is tuned by changing the amount of glycerol in the hydrothermal process. Glycerol can induce the ordered assembly of TiO$_2$ during the hydrothermal process, and part of C can be incorporated into the TiO$_2$ lattice after its decomposition during high-temperature calcination. Surprisingly, the obtained defect-rich Ni-Cr(OH)$_3$/C-TiO$_2$ catalyst shows high catalytic performance and remarkable durability for hydrogen production from N$_2$H$_4$·H$_2$O. The TOF value of Ni-Cr(OH)$_3$/C-TiO$_2$ reached as high as 266 h^{-1} at 323 K, and the catalyst performance did not decrease significantly even after 20 cycles, which is one of the best reports on noble-metal-free catalysts to date. In addition, Ni-Cr(OH)$_3$/C-TiO$_2$ catalyst also showed excellent catalytic efficiency (577 h^{-1}) and robust durability for the dehydrogenation of N$_2$H$_4$BH$_3$.

2. Experimental

2.1. Synthetic procedure

C-doped TiO$_2$ nanosheets with different C doping amounts were synthesized by a solvent-induced hydrothermal method combined with high temperature calcination, where the C doping amount of C-TiO$_2$ was controlled by changing the amount of glycerol ($x = 10$–50 mL) in the hydrothermal process (details are described in the Supporting Information). Ni-Cr(OH)$_3$ supported on C-TiO$_2$ was synthesized by a simple wet chemical method. Typically, C-TiO$_2$ (30 mg) is dispersed in 5 mL of deionized water, and then NiCl$_2$·6 H$_2$O (0.2 mmol, 48.4 mg) and Cr (NO$_3$)$_3$·9 H$_2$O (0.015 mmol, 6.0 mg) are added to the C-TiO$_2$ suspension and ultrasonic treatment is conducted at room temperature for 30 min. Then, quickly add 30 mg of NaBH$_4$ and stir vigorously. Finally, the black solid (Ni-Cr(OH)$_3$/C-TiO$_2$) was obtained until bubble formation stopped. As a comparison, Ni/C-TiO$_2$, Ni-Cr(OH)$_3$ NPs, and Ni NPs samples were synthesized using a similar way, with the difference being that C-TiO$_2$ and/or Cr(NO$_3$)$_3$ were not added. The Ni/TiO$_2$ and Ni-Cr (OH)$_3$/TiO$_2$ were prepared using the same method as that of Ni-Cr (OH)$_3$/C-TiO$_2$ except that TiO$_2$ nanosheets were used instead of C-TiO$_2$ nanosheets.
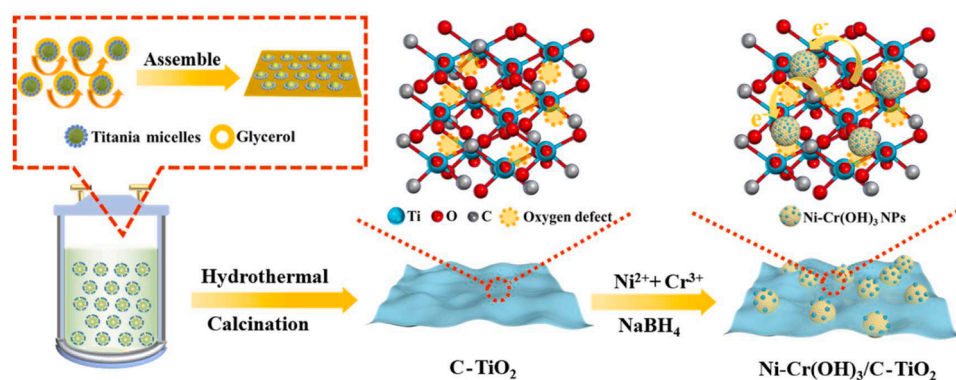
2.2. Catalytic activity measurement

The reaction device for measuring N$_2$H$_4$·H$_2$O gas production is the same as described in our previous work [62]. Usually, a catalyst suspension solution (10 mL) in the two-neck round-bottomed flask (50 mL). One of the two necks is used to connect the gas burette to the measure the volume of released gas. The other neck is used to inject 100 μL of N$_2$H$_4$·H$_2$O into the catalyst suspension under stirring, and the decomposition reaction begins. The volume of gas released is measured by recording the displacement of water in the gas burette. The content of Ni was fixed to be nNi/nN$_2$H$_4$·H$_2$O of 0.1 for all the catalysts. Immerse the flask in a constant temperature water bath.

3. Results and discussion

3.1. Catalysts characterization

As shown in Scheme 1, Cr(OH)$_3$-modified Ni NPs supported on defect-rich C-doped mesoporous TiO$_2$ nanosheets (C-TiO$_2$) was synthesized by a simple and facile approach. First, C-TiO$_2$ was synthesized by solvent induced hydrothermal synthesis of precursor followed by calcination in N$_2$ atmosphere at 350 °C. The oxygen defect amount of C-TiO$_2$ can be controlled by adjusting the C doping amount, which is tuned by changing the amount of glycerol in the hydrothermal process. Then, the synthesized C-TiO$_2$ was dispersed in water by sonication. Subsequently, NiCl$_2$·6 H$_2$O and Cr(NO$_3$)$_3$·6 H$_2$O were added to the well-dispersed C-TiO$_2$ suspension and stirred for 30 min. Then, quickly add 30 mg of NaBH$_4$ and stir vigorously. Ni^{2+} is reduced to Ni^0 by NaBH$_4$, while Cr^{3+} cannot be reduced to Cr^0 because of the lower reduction potentials of Cr (III)/Cr(0) (E$^0_{Cr(III)/Cr(0)}$ = −0.74 eV vs SHE). The alkali solution generated in situ after hydrolysis of NaBH$_4$ converts it to Cr(OH)$_3$. The obtained catalyst Ni-Cr(OH)$_3$/C-TiO$_2$ was used for the following characterization and catalytic performance test. The Ni-Cr(OH)$_3$/C-TiO$_2$ synthesized with 40 mL glycerol exhibited the highest catalytic efficiency among all synthesized catalysts (vide infra). Therefore, if the dosage of glycerol used in the catalyst is not specified in the article, it refers to the use of 40 mL of glycerol during the synthesis of precursors.

The structure and morphology of the synthesized catalyst were characterized by scanning electron microscopy (SEM) and transmission electron microscopy (TEM). As shown in Figs. 1a and S1, the mesoporous C-TiO$_2$ is a flower-like structure formed by stacking two-dimensional nanosheets. After loading Ni-Cr(OH)$_3$ NPs on mesoporous C-TiO$_2$ nanosheets, the shape of the Ni-Cr(OH)$_3$/C-TiO$_2$ still maintains

Scheme 1. Schematic illustration of the preparation of Ni-Cr(OH)$_3$/C-TiO$_2$.
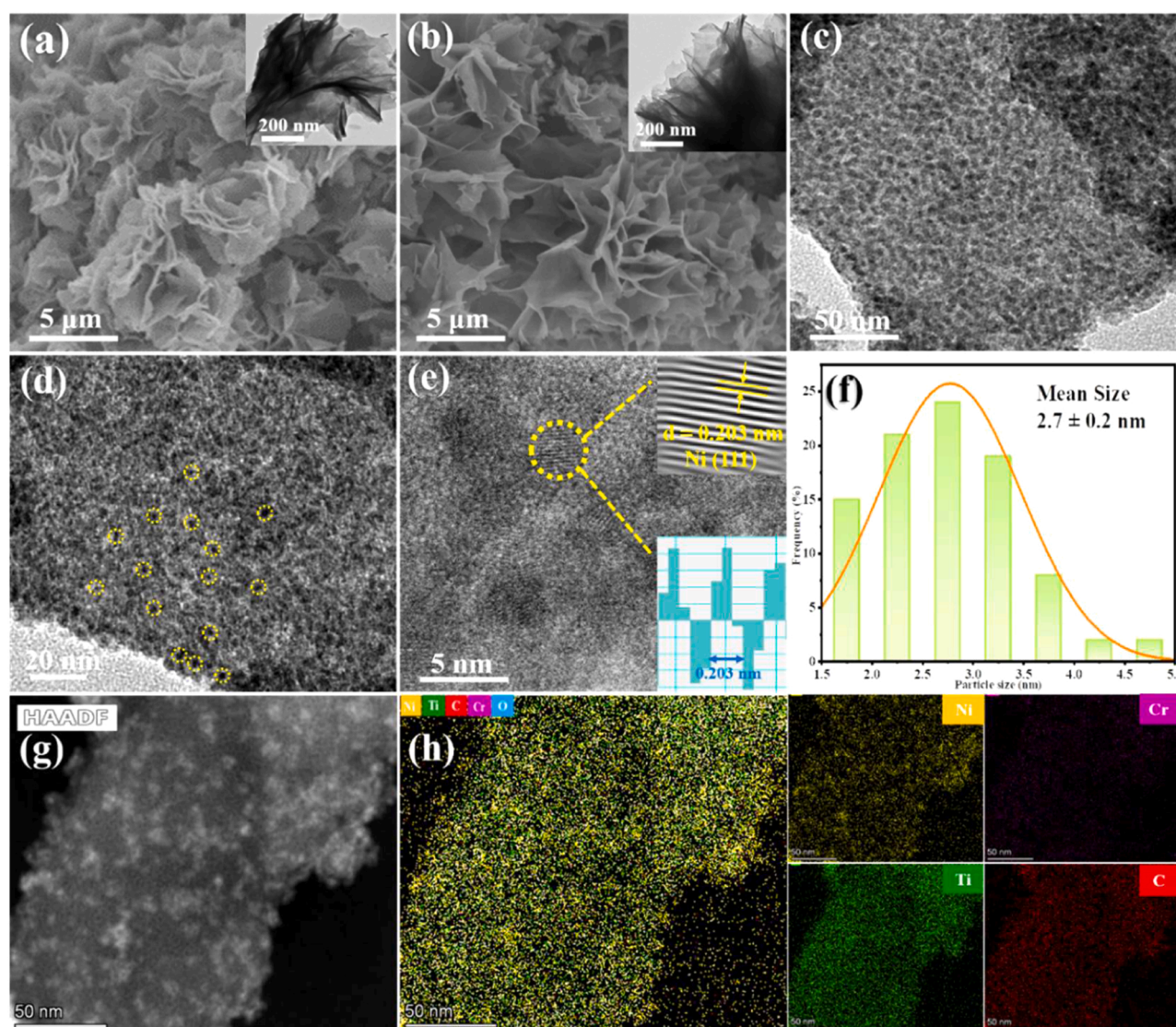

Fig. 1. SEM images of (a) C-TiO$_2$ and (b) Ni-Cr(OH)$_3$/C-TiO$_2$ (inset: the corresponding TEM images); (c,d) TEM images, (e) HRTEM image (inset: the corresponding inverse FFT patterns), (f) particle size distribution, and (g) HAADF-STEM image of Ni-Cr(OH)$_3$/C-TiO$_2$; (h) The corresponding EDS mapping images of Ni, Cr, Ti, and C.

the original flower-like structure (Fig. 1b). Additionally, Ni-Cr(OH)$_3$ NPs with an average size of 2.7 nm is uniformly dispersed on the nanosheets of C-TiO$_2$ (Fig. 1c-e). High-resolution TEM image in Ni-Cr(OH)$_3$/C-TiO$_2$ shows lattice fringes of 0.203 nm, corresponding to the face-centered cubic Ni (111) plane (inset of Fig. 1e). The ICP-OES analysis results of Ni-Cr(OH)$_3$/C-TiO$_2$ showed that the actual loadings of Ni and Cr are 23.5 and 1.5 wt%, respectively, close to the theoretical values (Table S1). The TG analysis reveals that the C content in C-TiO$_2$ is about

28.9 wt% (Fig. S2). In addition, the uniform dispersion of Ni, Cr, Ti, and C in the Ni-Cr(OH)$_3$/C-TiO$_2$ was further confirmed by the corresponding EDS elemental mappings (Fig. 1g and h). In contrast, compared with Ni-Cr(OH)$_3$/C-TiO$_2$, Ni-Cr(OH)$_3$ NPs loaded on TiO$_2$ nanosheets without C doping (Ni-Cr(OH)$_3$/TiO$_2$) show larger particle size of 5.6 nm (Fig. S3), which reflected the key role of C doped TiO$_2$ in regulating the particle size and dispersion of metal NPs. Besides the support, adding transition metal to modify Ni NPs can also regulate its particle size. As shown in Fig. S4, the size of Ni NPs in Ni/C-TiO$_2$ prepared without Cr (3.3 nm) is relatively larger than that of Ni-Cr(OH)$_3$/C-TiO$_2$ prepared with Cr (2.7 nm), indicating Cr(OH)$_3$ can serve as an atomic barrier to inhibit the growth of Ni NPs. Ni-Cr(OH)$_3$ NPs without C-TiO$_2$ are severely agglomerated to a large size (12.3 nm). Therefore, the introduction of C-TiO$_2$ and Cr(OH)$_3$ contributes to form highly dispersed and small-sized Ni NPs.

The crystal structures of the catalysts were characterized by X-ray diffraction (XRD). In Fig. 2a, all diffraction peaks of Ni-Cr(OH)$_3$/TiO$_2$ can be regarded as a tetragonal phase, corresponding to anatase TiO$_2$ (JCPDS: 21–1272) [63]. However, Ni-Cr(OH)$_3$/C-TiO$_2$ shows a wide low crystal diffraction peak, which may be due to the limitation of the uniform dispersion of TiO$_2$ in the carbon agent, resulting in a small crystal size. It is worth noting that the characteristic diffraction peaks related to Ni and/or Cr(OH)$_3$ species are not shown in Ni-Cr(OH)$_3$/C-TiO$_2$ and Ni/C-TiO$_2$ (Fig. S5), which is possibly attributed to their high dispersion and small size. While for Ni and Ni-Cr(OH)$_3$ NPs without support, there is a central peak located at 44.5°, which belongs to the (111) plane of face-centered cubic (fcc) Ni (JCPDS: 04–0850), indicating that Ni and

Ni-Cr(OH)$_3$ have crystalline structures.

Fig. S6 shows the N$_2$ adsorption-desorption isotherms of Ni-Cr(OH)$_3$ loaded on C-TiO$_2$ and TiO$_2$ respectively. It can be clearly observed that the two catalysts show the characteristics of type IV isotherm with H$_2$ hysteresis ring, which indicates that they have mesoporous structure. Compared with Ni-Cr(OH)$_3$/TiO$_2$, the specific surface area and pore volume of Ni-Cr(OH)$_3$/C-TiO$_2$ are larger and the pore size is smaller, indicating that the incorporation of C into TiO$_2$ increases the specific surface area to a certain extent, while the reduction of pore size indicates that the incorporation of C is successful. The decrease of specific surface area of Ni-Cr(OH)$_3$/C-TiO$_2$ relative to C-TiO$_2$ may be due to the fact that the loading of Ni-Cr(OH)$_3$ occupies a certain area (Table S2), which again proves that the metal NPs are well loaded.

To prove the introduction of defects in Ni-Cr(OH)$_3$/C-TiO$_2$, Raman spectroscopy was performed. The Ni-Cr(OH)$_3$/C-TiO$_2$ exhibits typical D-band (1348 cm^{-1}) and G-band (1582 cm^{-1}) (Fig. 2b), respectively, which attributes to the carbon defects and ordered graphitic structure. However, Ni-Cr(OH)$_3$/TiO$_2$ without C doping shows no such peaks. Furthermore, after C incorporation into TiO$_2$, the Raman signal of TiO$_2$ is attenuated and broadened, confirming the weakening of the symmetric stretching vibration of the Ti-O-Ti bond. Additionally, the E$_g$ band of Ni-Cr(OH)$_3$/C-TiO$_2$ (151 cm^{-1}) is blue shifted compared to that of Ni-Cr(OH)$_3$/TiO$_2$ (143 cm^{-1}), indicating that a Ti^{3+}/OVs-related disordered structure is formed during self-doping process [64]. The above results reveal that the original symmetry TiO$_2$ lattice is broken to form non-stoichiometric TiO$_{2-x}$, and the blue shift of Ni-Cr(OH)$_3$/C--TiO$_2$ also verifies the strong interaction between C and TiO$_2$.
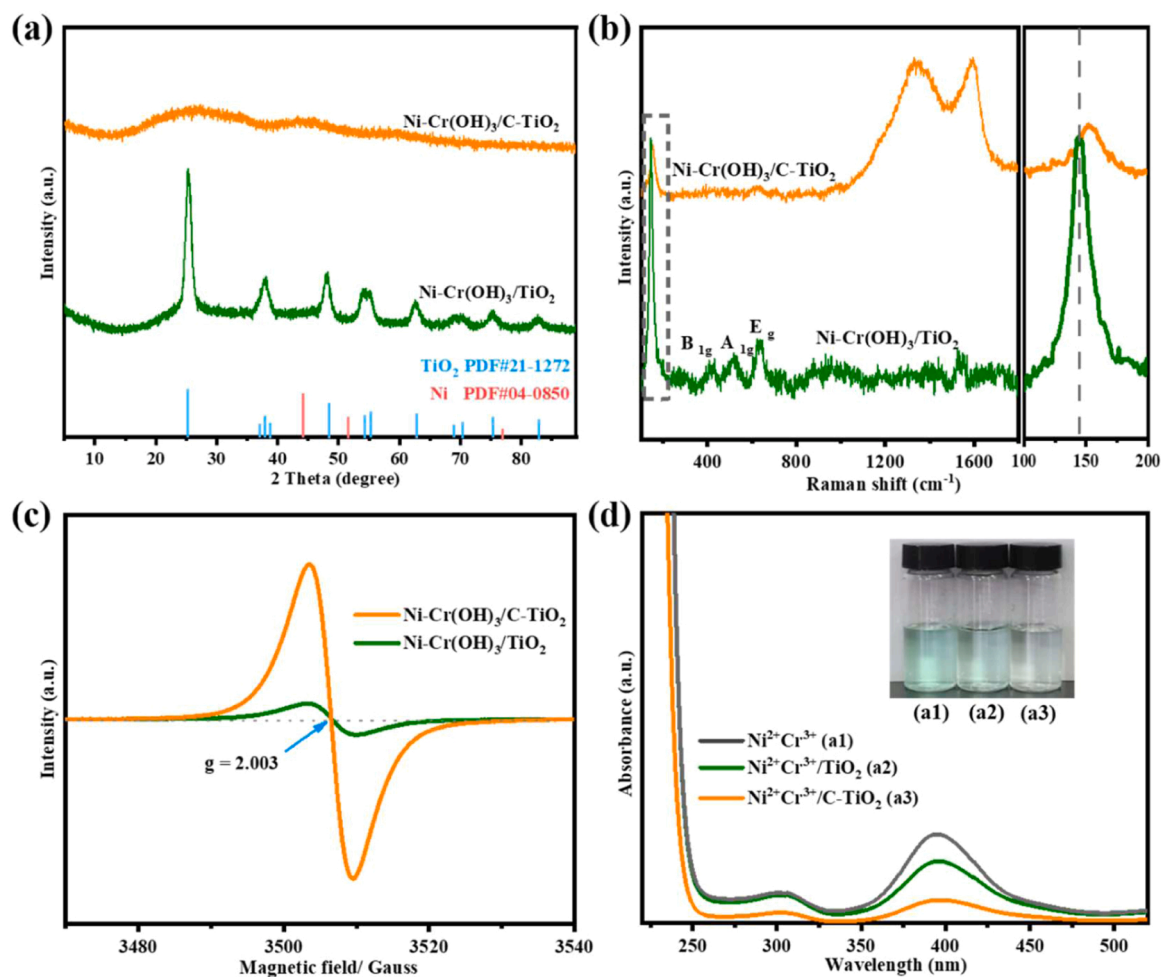

Fig. 2. (a) XRD patterns, (b) Raman spectra, and (c) EPR spectra of Ni-Cr(OH)$_3$/TiO$_2$ and Ni-Cr(OH)$_3$/C-TiO$_2$; (d) UV–Vis spectra of (a1) Ni^{2+}Cr^{3+}, (a2) Ni^{2+}Cr^{3+}/TiO$_2$, and (a3) Ni^{2+}Cr^{3+}/C-TiO$_2$ aqueous solution after mixing and standing for 12 h, the inset is corresponding photos.

To further demonstrate the existence of oxygen defects in Ni-Cr (OH)$_3$/C-TiO$_2$, electron paramagnetic resonance (EPR) was performed. As shown in Fig. 2c, it can be seen that C-doped TiO$_2$ has a peak at g value of 2.003, which is a characteristic peak of oxygen defect, and its signal intensity can be found to be significantly stronger than TiO$_2$. Because when C is doped into TiO$_2$, its internal structure will be disordered, resulting in a large number of oxygen defects [65]. The C-TiO$_2$ with abundant oxygen defects is not only conducive to the adsorption of metal ions to obtain highly dispersed small-sized metal NPs, but also regulate the electronic structure of the active metal to make its surface electron-rich state. The chemical structure of the catalysts was further analyzed by Fourier transform infrared spectroscopy (FTIR). As shown in Fig. S7, the peaks at 3422 and 1631 cm^{-1} are corresponded to the -OH vibration, and the peak at 400–700 cm^{-1} is assigned to the Ti-O-Ti bridge stretching modes. In addition, the Ti-O-Ti peak of Ni-Cr (OH)$_3$/C-TiO$_2$ is broader than that of Ni-Cr(OH)$_3$/TiO$_2$, because the doping of C leads to the disorder of self-doping, thus weakening the tensile strength of Ti-O-Ti [66].

In order to explore the effect of defects in the C-TiO$_2$ on the adsorption capacity of metal ions, we took photos to observe the color changes of the supernatant after the adsorption of metal ions on different supports. As shown in Fig. 2d (inset), the supernatant of the mixed solution of Ni^{2+}, Cr^{3+}, and TiO$_2$ after standing for 12 h is light green, which is close to the color of Ni^{2+} and Cr^{3+} aqueous solution; while the supernatant of the mixed solution of Ni^{2+}, Cr^{3+}, and C-TiO$_2$ after standing for 12 h is colorless and transparent. These results indicate that C-TiO$_2$ with abundant oxygen defects has much stronger adsorption

capacity for Ni^{2+} and Cr^{3+} than TiO$_2$. Moreover, UV-Vis absorption spectroscopy was further performed to analyze the supernatant of the above three samples. As shown in Fig. 2d, in the absence of support materials, the mixed solution of Ni^{2+} and Cr^{3+} appear absorption peak at around 390 nm. The intensity absorption peak of the supernatant of Ni^{2+} and Cr^{3+} mixed with C-TiO$_2$ after standing is very weak compared to that of the supernatant of Ni^{2+} and Cr^{3+} mixed with TiO$_2$, which confirms that C-TiO$_2$ has a stronger ability to adsorb metal ions and is consistent with the corresponding color changes. The enhanced adsorption capacity of C-TiO$_2$ is due to the increase in the number of defects on the surface of TiO$_2$, with a large number of unsaturated sites making it easier to absorb metal ions, thus facilitating the preparation of highly dispersed and small-sized metal NPs, as confirmed by TEM analysis.

The compositions and chemical states of the catalysts were studied using X-ray photoelectron spectroscopy (XPS). The full spectrum of Ni-Cr(OH)$_3$/C-TiO$_2$ proves the presence of Ni, Cr, Ti, O, and C elements (Fig. S8). As shown in Fig. 3a, the high-resolution Ti 2p XPS spectrum of Ni-Cr(OH)$_3$/TiO$_2$ is deconvolved into two Ti^{4+} peaks (458.9 and 464.5 eV). The high-resolution Ti 2p XPS spectrum of Ni-Cr(OH)$_3$/C-TiO$_2$ are deconvolved into four peaks, two peaks of 459.4 and 465.3 eV are attributed to Ti^{4+} 2p$_{3/2}$ and Ti^{4+} 2p$_{1/2}$, and the other two peaks of 457.5 and 463.7 eV are assigned to Ti^{3+} 2p$_{3/2}$ and Ti^{3+} 2p$_{1/2}$, confirmed that Ti^{3+} species were formed after incorporation of C. Meanwhile, compared with Ni-Cr(OH)$_3$/TiO$_2$, the binding energies of Ti^{4+} 2p$_{3/2}$ and Ti^{4+} 2p$_{1/2}$ of Ni-Cr(OH)$_3$/C-TiO$_2$ display a positive shifted, which may be attributed to the strong electronic effect and/or interactions between
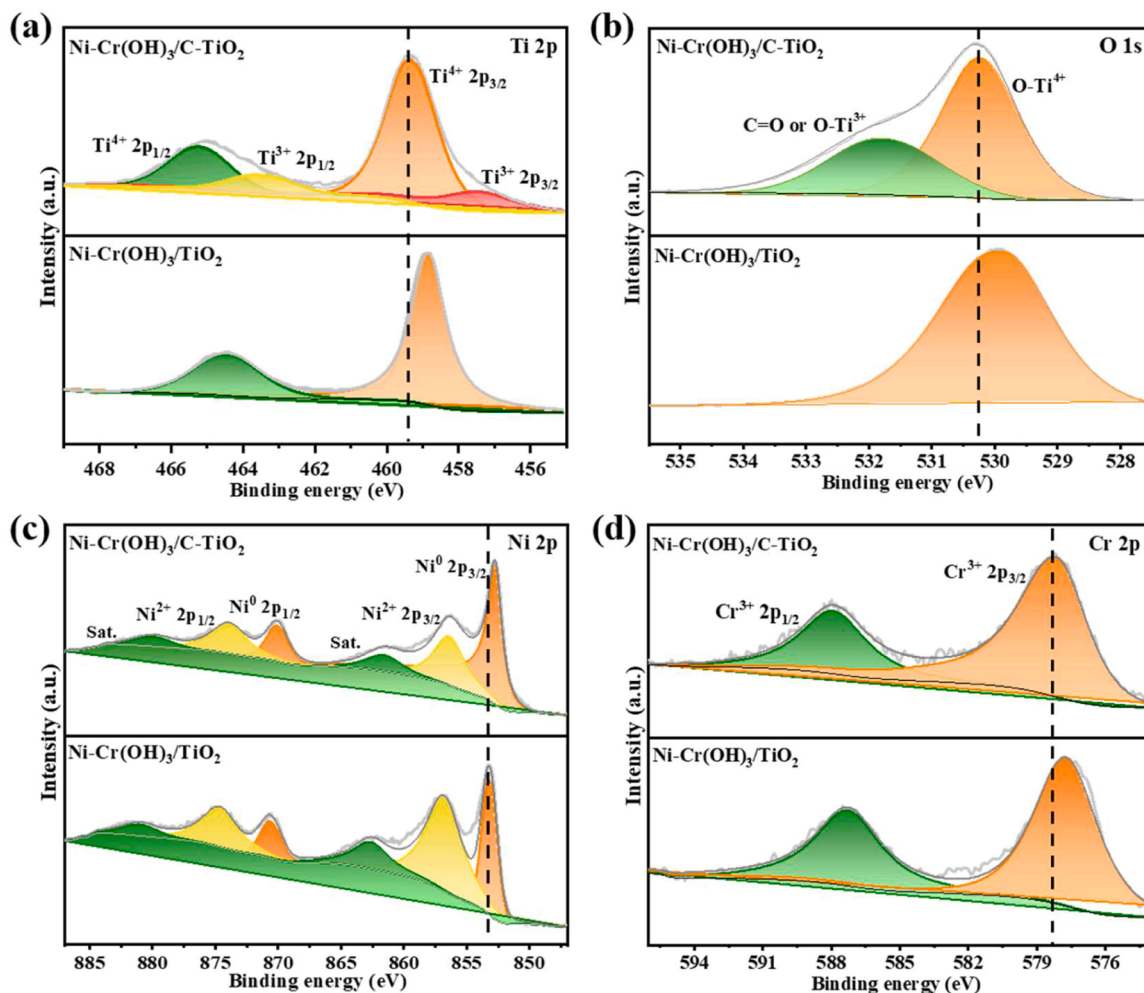

Fig. 3. XPS spectra of (a) Ti 2p, (b) O 1 s, (c) Ni 2p, and (d) Cr 2p of the synthesized catalysts.

TiO$_2$ and C in Ni-Cr(OH)$_3$/C-TiO$_2$. The O1s XPS spectrum of Ni-Cr(OH)$_3$/C-TiO$_2$ reveals the presence of O-Ti^{4+} groups (530.3 eV), O-Ti^{3+} groups (531.8 eV), or C=O. Additionally, the binding energy of O-Ti^{4+} groups in Ni-Cr(OH)$_3$/C-TiO$_2$ is positively shifted relative to Ni-Cr(OH)$_3$/TiO$_2$, furthering indicating the existence of oxygen defects on Ni-Cr(OH)$_3$/C-TiO$_2$. The Ni 2p$_{3/2}$ spectrum of Ni-Cr(OH)$_3$/C-TiO$_2$ exhibits a peak attributed to metal Ni (0) at approximately 852.8 eV (Fig. 3c), and the peak of Ni 2p$_{3/2}$ at 856.5 eV belongs to Ni^{2+}, which may be due to partial oxidation of the catalyst during the sample preparation process [67]. Its satellite peak is approximately at 861.7 eV of Ni 2p$_{3/2}$ peak. Additionally, the Ni 2p$_{3/2}$ peak of the Ni-Cr(OH)$_3$/C-TiO$_2$ is shifted to lower binding energy in comparison to those of Ni-Cr(OH)$_3$/TiO$_2$ (853.3 eV). Compared with Ni-Cr(OH)$_3$ NPs (Fig. S9, 853.7 eV) and Ni/C-TiO$_2$ (Fig. S9, 853.1 eV), the binding energy of metal Ni in Ni-Cr(OH)$_3$/C-TiO$_2$ is also shifted to a lower value. The above result indicates that some electrons transferred from C-TiO$_2$ and Cr(OH)$_3$ to Ni. For the Cr 2p of Ni-Cr(OH)$_3$/C-TiO$_2$ (Fig. 3d), the binding energy difference between Cr^{3+} peaks (2p$_{1/2}$ and 2p$_{3/2}$) is 9.8 eV, which indicates that Cr elements exits as Cr(OH)$_3$ [68]. The exist of Cr(OH)$_3$ can increase the basic sites in the catalyst and adjust the microscopic pH of the Ni surface. Moreover, compared with Ni-Cr(OH)$_3$/TiO$_2$ (577.8 eV), the binding energy of Cr^{3+} 2p$_{3/2}$ in Ni-Cr(OH)$_3$/C-TiO$_2$ is shifted to a higher value (578.3 eV), suggesting the transfer of some electrons from Cr(OH)$_3$ to C-TiO$_2$. The above XPS analysis results indicated that the incorporation of C into support TiO$_2$ and the addition of Cr into metal Ni can increase the electron density of the active metal Ni surface, which is beneficial for promoting the breaking of the N-H bond, thus improving catalytic efficiency [69].

3.2. Catalytic activity

The catalytic activities of the as-prepared catalysts toward the dehydrogenation of N$_2$H$_4$·H$_2$O were tested in a typical water-filled graduated burette system at 323 K. As shown in Fig. 4a, the Ni-Cr(OH)$_3$ NPs supported on mesoporous TiO$_2$ nanosheets (Ni-Cr(OH)$_3$/TiO$_2$) displays a low catalytic activity for N$_2$H$_4$·H$_2$O dehydrogenation, with which 3.0 equivalent of (N$_2$ + H$_2$) per N$_2$H$_4$ (α = 100%) were generated within 29.4 min at 323 K. In contrast, the catalytic activity of Ni-Cr(OH)$_3$ NPs supported on C-doped mesoporous TiO$_2$ nanosheets (Ni-Cr(OH)$_3$/C-TiO$_2$) is significantly enhanced, with the complete dehydrogenation of N$_2$H$_4$·H$_2$O takes only 4.5 min at 323 K. The reaction completeness was characterized by UV-Vis spectroscopy. As displayed in Fig. S10, the liquid after complete reaction showed no adsorption peak at 458 nm by UV-Vis detection, indicating 100% conversion of N$_2$H$_4$. The generated gas from N$_2$H$_4$ decomposition over Ni-Cr(OH)$_3$/C-TiO$_2$ is identified as a mixture of only H$_2$ and N$_2$ by gas chromatography (GC) (Fig. S11), indicating 100% H$_2$ selectivity. The Ni-Cr(OH)$_3$/C-TiO$_2$ catalyst after the dehydrogenation reaction was analyzed by N$_2$ adsorption-desorption isotherms (Fig. S12) and FTIR spectroscopy (Fig. S13), and the results show that the specific surface area, pore
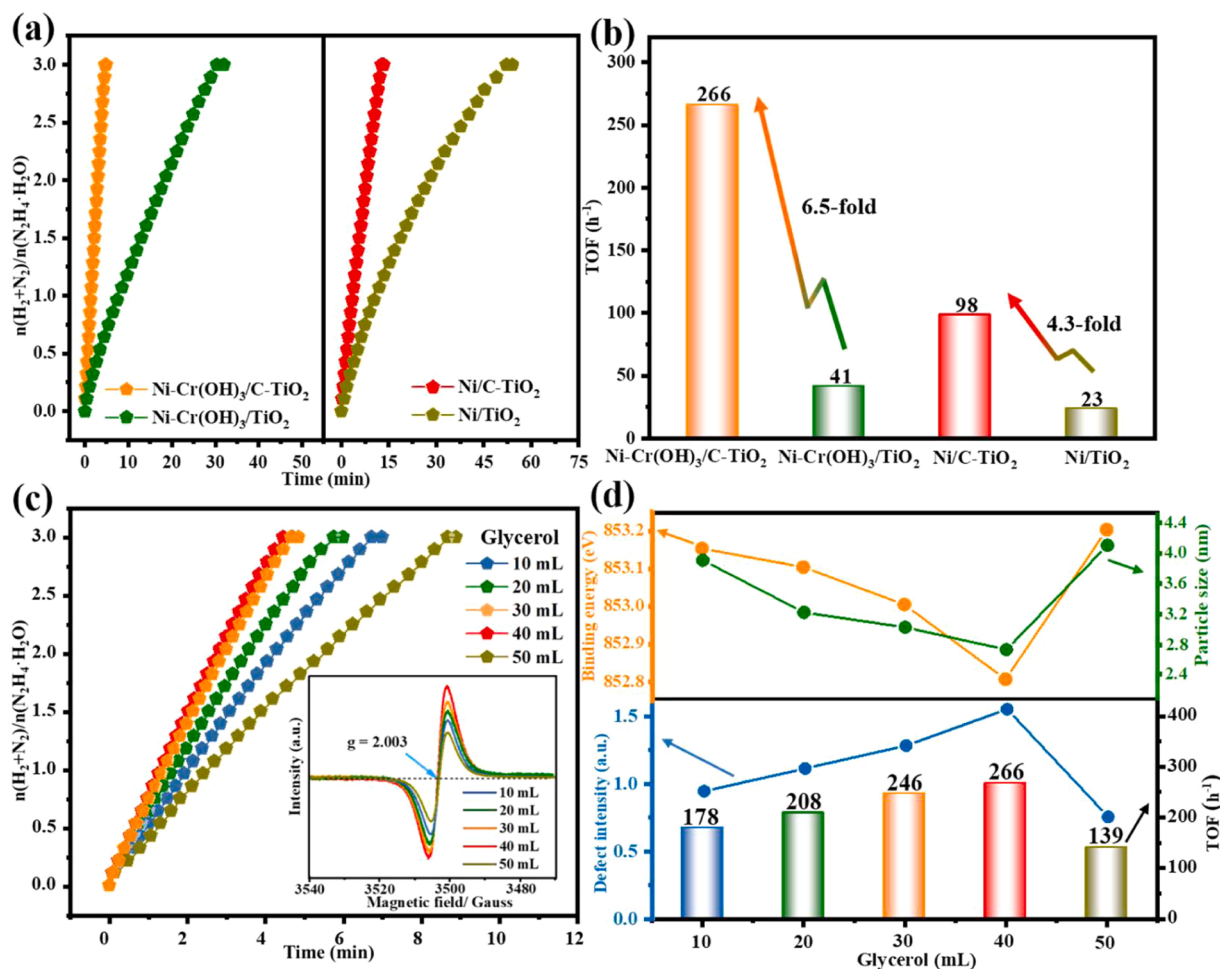

Fig. 4. Hydrogen evolution time course plots of N$_2$H$_4$·H$_2$O (0.2 M, 5 mL) catalyzed by (a) Ni-Cr(OH)$_3$/C-TiO$_2$, Ni-Cr(OH)$_3$/TiO$_2$, Ni/C-TiO$_2$, and Ni/TiO$_2$, (b) the corresponding TOF values, and (c) Ni-Cr(OH)$_3$/C-TiO$_2$-x prepared with different amounts of glycerol (x = 10–50 mL) with NaOH (3.0 M) at 323 K ($n_{Ni}/n_{N2H4·H2O}$ = 0.1). Inset of (c) is the corresponding EPR spectra. (d) The correlation between the amount of oxygen vacancy, the particle size of Ni NPs, the binding energy of Ni, and the corresponding TOF value of Ni-Cr(OH)$_3$/C-TiO$_2$ prepared with different amounts of glycerol.

volume, and pore size, and chemical structure of catalyst did not change significantly, indicating its structural stability. The TOF value of Ni-Cr$(OH)_3$/C-TiO$_2$ is determined to be 266 h^{-1}, which is 6.5 times higher than Ni-Cr(OH)$_3$/TiO$_2$ (41 h^{-1}) and one of the highest values reported so far for noble-metal-free catalysts (Table S3). The obvious difference in activity reflects the significant impact of introducing C into TiO$_2$ to produce oxygen defects on catalytic activity. The superior catalytic efficiency is mainly because of the small-sized and electron-rich of Ni NPs induced by the oxygen defects of C-TiO$_2$.

Compared with Ni/TiO$_2$, there is also a similar improvement in catalytic performance in Ni/C-TiO$_2$ (Fig. 4a and b). The TOF value of Ni/C-TiO$_2$ (98 h^{-1}) is 4.3 times that of Ni/TiO$_2$ (23 h^{-1}) at 323 K, confirming that introducing oxygen defects into TiO$_2$ is a universal and effective method to improve the catalytic performance. Notably, C-TiO$_2$ is inactive in N$_2$H$_4$·H$_2$O dehydrogenation (Fig. S14). The activity activities of commercial anatase TiO$_2$-supported Ni-Cr(OH)$_3$ (44.3 h^{-1}, $\alpha = 100\%$), support-free Ni-Cr(OH)$_3$ (50 h^{-1}, $\alpha = 81.3\%$), and Ni NPs (6 h^{-1}, $\alpha = 36.6\%$) are far lower than that of Ni-Cr(OH)$_3$/C-TiO$_2$ catalyst (Fig. S15). Additionally, compared to Ni/C-TiO$_2$, the obtained Ni-MoO$_x$/C-TiO$_2$ and Ni-WO$_x$/C-TiO$_2$ show higher catalytic activity, but not as good as Ni-Cr(OH)$_3$/C-TiO$_2$ (Fig. S16). In addition, the effect of different amounts of doping Cr(OH)$_3$ and support C-TiO$_2$ on the catalyst performance was also explored. The optimal amount of nCr/n(Cr + Ni) (Fig. S17) and C-TiO$_2$ (Fig. S18) are 7.5% and 30 mg, respectively. Furthermore, the optimal concentration of NaOH is 3.0 M (Fig. S19), but only NaOH solution does not catalyze the dehydrogenation of N$_2$H$_4$, indicating that NaOH is used as a promoter rather than a catalyst (Fig. S20). The promotion mechanism of NaOH may be due to the fact that the presence of NaOH can effectively reduce the undesired N$_2$H$_5^+$ (N$_2$H$_5^+$ + OH$^-$ → N$_2$H$_4$ + H$_2$O) and accelerate the rate determination step to proceed (N$_2$H$_4$ → N$_2$H$_3$ * + H*), thereby promoting reaction kinetics. In addition, the presence of NaOH can also suppress the release of byproduct NH$_3$.

In order to further investigate the effect of oxygen defect amount of C-TiO$_2$ on the catalyst performance, Ni-Cr(OH)$_3$ NPs supported on C-TiO$_2$-x with different C doping amounts were synthesized. The C doping amount was controlled by changing the amount of glycerol ($x = 10$–50 mL) in the hydrothermal process. As shown in Fig. 4c, when the amount of glycerol increased from 10 to 40 mL, the catalytic activity of Ni-Cr(OH)$_3$/C-TiO$_2$ gradually enhanced, and the TOF values increased from 178 h^{-1} to 266 h^{-1} (Fig. 4d). However, when the amount of glycerol was further increased to 50 mL, the catalytic activity decreased significantly (139 h^{-1}). From the TG and EPR analysis, it can be seen that with the increase of glycerol content (10–40 mL), the C doping amount gradually increased (21.4%−28.9%, Fig. S21), and the signal of oxygen defects became stronger and stronger (Fig. 4c), indicating that with the increase of C doping amount, more and more oxygen defects in C-TiO$_2$. When glycerol was further increased to 50 mL, the C doping amount is further increased (41.2%), but the oxygen defect amount decreases sharply, because too many C atoms will occupy most of the oxygen atoms, and TiO$_2$ will be covered by the C layer, resulting in a decrease in catalytic performance. Previous theoretical works also showed that the amount of oxygen defect in TiO$_2$ can be adjusted by carbon doping [70]. Notably, the different oxygen defect amounts of C-TiO$_2$ obtained here are relative change amount. The amount of oxygen defects cannot be accurately quantified because the values obtained by EPR characterization are relative quantities. It is well known that accurately quantifying defects is very difficult at present [71]. In this regard, we need to find suitable experimental methods and characterization techniques combined with theoretical calculations to quantify the defect amount of catalyst in future work.

We further analyzed the effect of oxygen defects on metal ion adsorption, metal dispersion and size as well as electronic structure using UV-Vis, TEM, and XPS techniques. From the UV-Vis and TEM analysis, it can be seen that with the increase the amount of oxygen defect in C-TiO$_2$, the absorption ability to metal Ni ions increases

(Fig. S22), and the particle size of Ni NPs decreases (4.1–2.7 nm, Fig. S23). Moreover, from the XPS analysis (Fig. S24), it can be seen that with the increase the amount of oxygen defect in C-TiO$_2$, the binding energies of metal Ni decrease (853.2–852.8 eV), indicating that the electron density of metal Ni increases. As a result, among the investigated catalysts, the Ni-Cr(OH)$_3$/C-TiO$_2$-40 has the highest defect amount, the smallest metal particle size, the highest metal electron density, showing the highest catalytic performance. The more oxygen defects, the better the catalytic activity. In view of excellent catalytic activity of defect-rich Ni-Cr(OH)$_3$/C-TiO$_2$ in the dehydrogenation of N$_2$H$_4$ aqueous solution, it is expected that this catalyst can also be used to efficiently removal N$_2$H$_4$ from sewage, which is conducive to promoting the sustainable development of the environment [72,73].

To further study the kinetic information of N$_2$H$_4$ dehydrogenation over Ni-Cr(OH)$_3$/C-TiO$_2$, the influences of N$_2$H$_4$ concentration, catalyst concentration, and reaction temperature were studied. As shown in Fig. S25a, the rate of H$_2$ generation does not increase with the increase of N$_2$H$_4$ concentration. Based on the plots of H$_2$ production rate and N$_2$H$_4$ concentration (both on a logarithmic scale), a straight line with a slope less than 0.1 is fitted, which means that the N$_2$H$_4$ dehydrogenation reaction is almost zero-order relative to the N$_2$H$_4$ concentration ranges from 0.2 to 0.8 M. As the concentration of Ni increases, the rate of H$_2$ generation increases accordingly (Fig. S25b). The curve graph (both logarithmic scale) based on H$_2$ production rate and catalyst concentration shows a straight line with a slope of 1.1, which means that N$_2$H$_4$ dehydrogenation is almost a first-order reaction relative to the catalyst concentration range of 0.02–0.05 M. As displayed in Fig. 5a, the activity of the catalyst increases with the increase of reaction temperature (303–343 K). The catalytic reactions for hydrogen generation from N$_2$H$_4$ over Ni-Cr(OH)$_3$/C-TiO$_2$ were completed within 21.1, 10, 4.5, 2.8, and 1.31 min at 303, 313, 323, 333, and 343 K, respectively, corresponding to TOF values of 57, 120, 266, 426, and 910 h^{-1} (Fig. 5b). According to the Arrhenius equation, the activation energy (E_a) of Ni-Cr(OH)$_3$/C-TiO$_2$ is calculated to be 52.6 kJ·mol^{-1}, which is lower than the majority of reported values for those catalysts in this reaction (Table S3). Additionally, the activation energies of Ni-Cr(OH)$_3$ NPs supported on C-TiO$_2$ prepared with 10, 20, 30, and 50 mL glycerol were also studied and calculated to be 58.6, 56.1, 53.4, and 60.9 kJ·mol^{-1} (Figs. 5c and S26), respectively, which is slightly higher than that of Ni-Cr(OH)$_3$ NPs supported on C-TiO$_2$ prepared with 40 mL glycerol. The activation energies of Ni-Cr(OH)$_3$/C-TiO$_2$ are consistent with their catalytic activities and confirmed that the more oxygen defects in Ni-Cr(OH)$_3$/C-TiO$_2$, the higher the catalyst activity and the lower reaction activation energy.

The stability of catalysts is also an important parameter in evaluating their sustainability and practicality in applications. In this study, after completing the previous run at 323 K, the durability of the catalysts was tested by adding the same amount of N$_2$H$_4$ to the reactor. The stability of Ni-Cr(OH)$_3$/C-TiO$_2$-x is related to the amount of glycerol ($x = 10$–50 mL) (Fig. 5d). Ni-Cr(OH)$_3$/C-TiO$_2$ was prepared with 40 mL glycerol showed the highest durability, with which retains ~59% of its initial catalytic activity (156 h^{-1}) and 100% H$_2$ selectivity even at the 20th cycle, which is significantly better than those of Ni-Cr(OH)$_3$/C-TiO$_2$ prepared the 10 mL (32.3%), 20 mL (36.2%), 30 mL (50.4%), and 50 mL (26.1%) of glycerol (Fig. S27). Clearly, the amount of oxygen defects in Ni-Cr(OH)$_3$/C-TiO$_2$ significantly affects the stability of the catalyst. The results show that the more oxygen defects, the better the catalyst stability. After 20 cycles, TEM images display that the particle size of Ni slightly increases from 2.7 to 4.6 nm (Fig. S28), which is responsible for its slightly decreased of its catalytic activity. Therefore, the robust durability of Ni-Cr(OH)$_3$/C-TiO$_2$ will help reduce the cost and consumption of catalysts, thereby promoting the development of clean energy technologies in practical applications.

Recently, hydrazine borane (N$_2$H$_4$BH$_3$, 15.4 wt%) has high hydrogen content and good stability at ambient temperature, it is regarded as another promising chemical hydrogen storage material [10,14,62]. When a suitable catalyst is used, the hydrogen stored in N$_2$H$_4$BH$_3$ can be
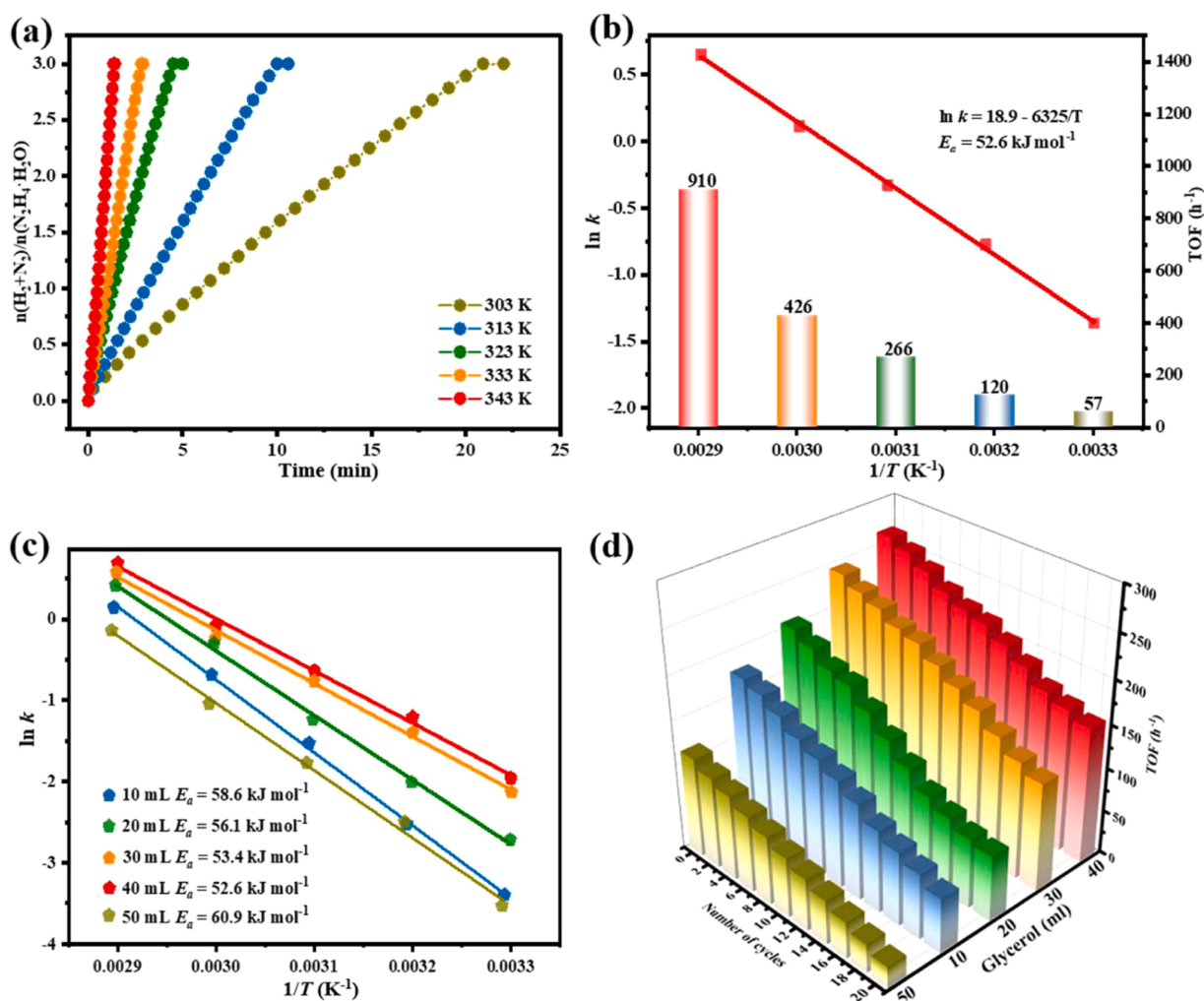
Fig. 5. (a) Hydrogen evolution time course plots of $N_2H_4 \cdot H_2O$ (0.2 M, 5 mL) at temperatures range of 303–343 K, (b) the related Arrhenius plot (ln k vs. 1000/T) and TOF values, (c) the corresponding Arrhenius plot (ln k vs. 1000/T), and (d) durability activities over Ni-Cr(OH)$_3$/C-TiO$_2$-x (x = 10–50 mL) prepared with different amounts of glycerol in the presence of NaOH (3.0 M) at 323 K ($n_{Ni}/n_{N2H4 \cdot H2O}$ = 0.1).

completely released ($N_2H_4BH_3(s) + 3 H_2O(l) \rightarrow B(OH)_3(l) + N_2(g) + 5 H_2(g)$) via the hydrolysis of the BH_3 group, and the decomposition of the N_2H_4 moiety. The synthesized Ni-Cr(OH)$_3$/C-TiO$_2$ in this work was subsequently applied to the dehydrogenation of $N_2H_4BH_3$. It is worth noting that among all the prepared catalysts, Ni-Cr(OH)$_3$/C-TiO$_2$ showed the highest activity (Fig. 6a), 6.0 equivalents (H$_2$ +N$_2$) were released per $N_2H_4BH_3$ within 2.6 min at 323 K. Clearly, the Ni-Cr(OH)$_3$/C-TiO$_2$ catalyst provided an exceptionally high TOF value of 577 h^{-1} at 323 K, which is about 4.7-fold higher than Ni-Cr(OH)$_3$/TiO$_2$ (121 h^{-1}) and is among the highest level reported so far for noble-metal-free catalysts (Table S4). Similarly, C-TiO$_2$ is also inactive in $N_2H_4BH_3$ dehydrogenation (Fig. S29). In addition, as shown in Fig. 6b, the dehydrogenation trend is similar to that of N_2H_4, the catalytic efficiency of Ni-Cr(OH)$_3$/C-TiO$_2$-x (x = 10–50 mL) for dehydrogenation $N_2H_4BH_3$ also increases with the increase of oxygen defect amount. The above results further demonstrate that the rich oxygen defects in Ni-Cr(OH)$_3$/C-TiO$_2$ can greatly enhance the catalytic efficiency.

Moreover, the effect of Ni-Cr(OH)$_3$/C-TiO$_2$ on the dehydrogenation rate of $N_2H_4BH_3$ was also investigated at different reaction temperatures. Similarly, as the reaction temperature increases, the catalytic hydrogen production rate also increases (Fig. 6c). Especially, the catalytic reaction of $N_2H_4BH_3$ for hydrogen production on Ni-Cr(OH)$_3$/C-TiO$_2$ was completed within 0.57 min at 343 K, and the TOF value

reached up to 2631 h^{-1}. By fitting the Arrhenius plots, it is calculated that the activation energy for hydrolysis of the BH_3 group corresponding to part 1 (E_{a1}) is 26.4 kJ mol^{-1}, and the activation energy for decomposition of the N_2H_4 group corresponding to part 2 (E_{a2}) is 54.8 kJ mol^{-1}. The durability of Ni-Cr(OH)$_3$/C-TiO$_2$ for $N_2H_4BH_3$ dehydrogenation were also investigated. Even after 20 cycles, the hydrogen selectivity of the Ni-Cr(OH)$_3$/C-TiO$_2$ for $N_2H_4BH_3$ dehydrogenation remained 100% (Fig. 6d), and the catalytic activity did not decrease significantly, further demonstrating the excellent durability of Ni-Cr(OH)$_3$/C-TiO$_2$ for hydrogen production reaction.

4. Conclusions

In summary, ultrafine and electron-rich Cr(OH)$_3$-modified Ni NPs (2.7 nm) supported on defect-rich C-doped mesoporous TiO$_2$ were successfully synthesized by impregnation reduction method. By simply changing the amount of carbon doping, the defect amount in C-TiO$_2$ can be easily adjusted. The characterization results show that abundant defects in C-TiO$_2$ can effectively disperse and reduce the size of metal NPs, increase the electron density of active metals, and thus improve the ability of catalyst to activate N-H bonds in $N_2H_4 \cdot H_2O$. Compared with Ni-Cr(OH)$_3$/TiO$_2$, the Ni-Cr(OH)$_3$/C-TiO$_2$ showed higher catalytic activity and 100% H$_2$ selectivity for hydrogen production from $N_2H_4 \cdot H_2O$ and $N_2H_4BH_3$ under alkaline conditions, providing TOF values up to
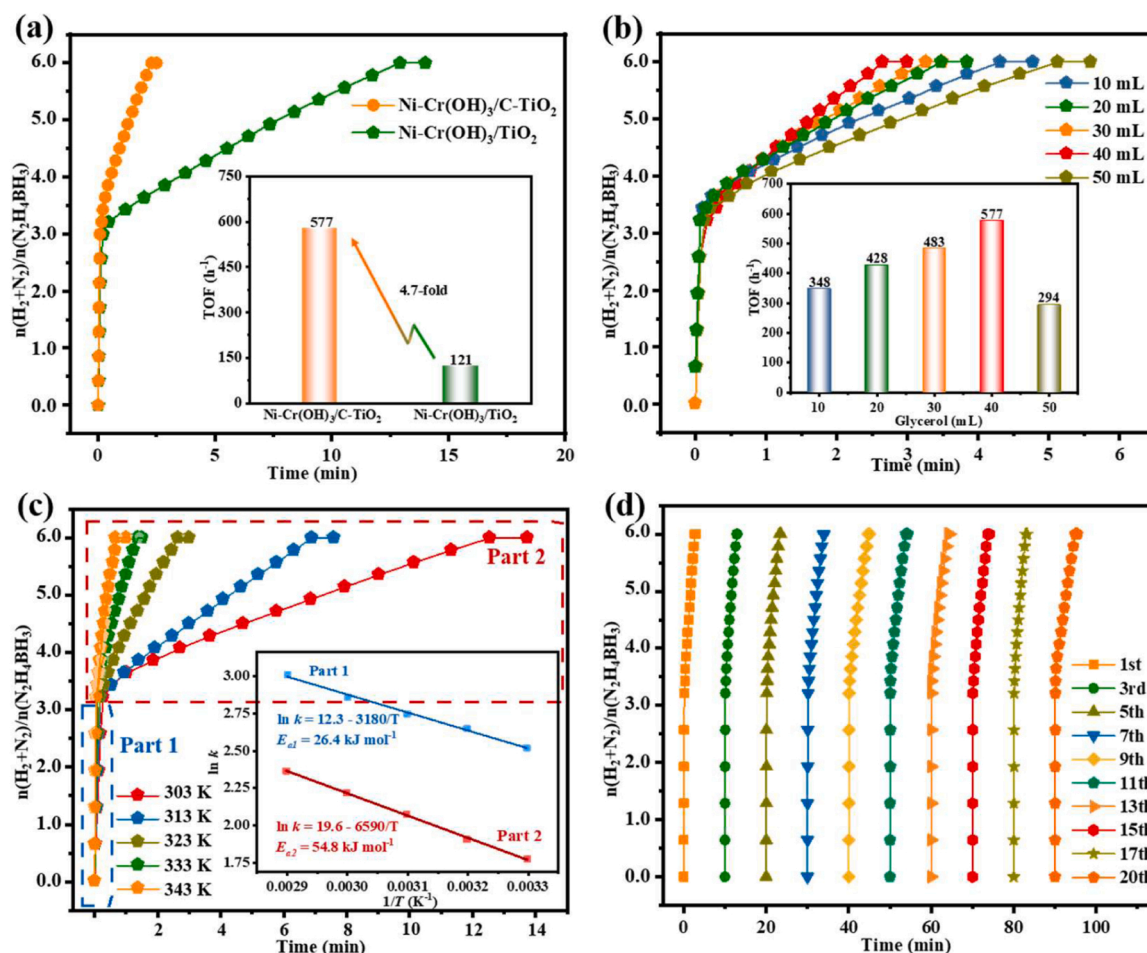
Fig. 6. Hydrogen evolution time course plots of $N_2H_4BH_3$ aqueous solution (0.2 M, 5 mL) catalyzed by (a) Ni-Cr(OH)$_3$/C-TiO$_2$ and Ni-Cr(OH)$_3$/TiO$_2$, (b) Ni-Cr(OH)$_3$/C-TiO$_2$-x ($x = 10$–50 mL) prepared with different amounts of glycerol with NaOH (3.0 M) at 323 K ($n_{Ni}/n_{N2H4BH3} = 0.2$). (c) Hydrogen evolution time course plots of $N_2H_4BH_3$ aqueous solution at temperatures range of 303–343 K (inset: Arrhenius plot versus 1000/T) and (d) Durability test over Ni-Cr(OH)$_3$/C-TiO$_2$ with NaOH at 323 K.

266 h^{-1} and 577 h^{-1} at 323 K, respectively, which is among the highest values ever reported for non-noble metal catalysts. Additionally, the Ni-Cr(OH)$_3$/C-TiO$_2$ catalyst also displayed robust durability without obvious degradation even after 20 cycles. The synthesized defect-rich Ni-Cr(OH)$_3$/C-TiO$_2$ catalyst has low cost, high activity, and high stability, which can promote the practical application of $N_2H_4 \cdot H_2O$ and $N_2H_4BH_3$ as hydrogen sources, as well as promote the sustainable development of clean energy and green chemicals. This study provides a novel and effective strategy for catalyst defect construction, and also opens up new avenues for the synthesis of defect-rich and efficient catalysts in other catalytic fields such as electrocatalysis photocatalysis.

CRediT authorship contribution statement

Xiaolei Zhang: Conceptualization, Investigation, Formal analysis, Writing – original draft. **Qilu Yao:** Investigation, Formal analysis, Writing – review & editing, Funding acquisition. **Haochong Wu:** Investigation. **Yuanlan Zhou:** Structure analysis. **Meihua Zhu:** Formal analysis. **Zhang-Hui Lu:** Conceptualization, Writing – review & editing, Validation, Supervision, Funding acquisition.

Declaration of Competing Interest

The authors declare that they have no known competing financial interests or personal relationships that could have appeared to influence the work reported in this paper.

Data availability

No data was used for the research described in the article.

Acknowledgments

Appendix A. Supporting information

Supplementary data associated with this article can be found in the online version at doi:10.1016/j.apcatb.2023.123153.

References

[1] Q.L. Zhu, Q. Xu, Liquid organic and inorganic chemical hydrides for high-capacity hydrogen storage, Energy Environ. Sci. 8 (2015) 478–512.

[2] Y. Li, H.H. Wang, C. Priest, S.W. Li, P. Xu, G. Wu, Advanced electrocatalysis for energy and environmental sustainability via water and nitrogen reactions, Adv. Mater. 33 (2021), 2000381.

[3] Y.L. Meng, Q.H. Sun, T.J. Zhang, J.C. Zhang, Z.Y. Dong, Y.H. Ma, Z.X. Wu, H. F. Wang, X.G. Bao, Q.M. Sun, J.H. Yu, Cobalt-promoted noble-metal catalysts for efficient hydrogen generation from ammonia borane hydrolysis, J. Am. Chem. Soc. 145 (2023) 5486–5495.

[4] J.K. Zhang, W.L. Yu, D. Feng, H. Xu, Y. Qin, Porous titania nanotube confined ultrafine platinum catalysts synthesized by atomic layer deposition with enhanced hydrolytic dehydrogenation performance, Appl. Catal. B Environ. 312 (2022), 121405.

[5] Q.M. Sun, N. Wang, Q. Xu, J.H. Yu, Nanopore-supported metal nanocatalysts for efficient hydrogen generation from liquid-phase chemical hydrogen storage Materials, Adv. Mater. 32 (2020) 2001818.

[6] W. Kang, A. Varma, Hydrogen generation from hydrous hydrazine over Ni/CeO$_2$ catalysts prepared by solution combustion synthesis, Appl. Catal. B Environ. 220 (2018) 409–416.

[7] P. Zhou, I.A. Navid, Y.J. Ma, Y.X. Xiao, P. Wang, Z.W. Ye, B.W. Zhou, K. Sun, Z. T. Mi, Solar-to-hydrogen efficiency of more than 9% in photocatalytic water splitting, Nature 613 (2023) 66–70.

[8] C.L. Wang, D. Astruc, Recent developments of nanocatalyzed liquid-phase hydrogen generation, Chem. Soc. Rev. 50 (2021) 3437–3484.

[9] A.Q. Zhang, J.H. Xia, Q.L. Yao, Z.H. Lu, Pd-WO$_x$ heterostructures immobilized by MOFs-derived carbon cage for formic acid dehydrogenation, Appl. Catal. B Environ. 309 (2022), 121278.

[10] J.J. Long, Q.L. Yao, X.L. Zhang, H.C. Wu, Z.H. Lu, Defects engineering of metal-organic framework immobilized Ni-La(OH)$_3$ nanoparticles for enhanced hydrogen production, Appl. Catal. B Environ. 302 (2023) 121989.

[11] C.Y. Shang, X. Xiao, Q. Xu, Coordination chemistry in modulating electronic structures of perovskite-type oxide nanocrystals for oxygen evolution catalysis, Coord. Chem. Rev. 485 (2023), 215109.

[12] Z. Chang, Y. Qiao, H.J. Yang, X. Cao, X.Y. Zhu, P. He, H.S. Zhou, Sustainable lithium-metal battery achieved by a safe electrolyte based on recyclable and low-cost molecular sieve, Angew. Chem. Int. Ed. 60 (2021) 15572–15581.

[13] Y. Wang, P.P. Du, H.Z. Pan, L. Fu, Y. Zhang, J. Chen, Y.W. Du, N.J. Tang, G. Liu, Increasing solar absorption of atomically thin 2D carbon nitride sheets for enhanced visible-light photocatalysis, Angew. Chem. Int. Ed. 31 (2019) 1807540.

[14] Q.L. Yao, X.L. Zhang, Z.H. Lu, Q. Xu, Metal-organic framework-based catalysts for hydrogen production from liquid-phase chemical hydrides, Coord. Chem. Rev. 493 (2023), 215302.

[15] C.G. Lang, Y. Jia, X.D. Yao, Recent advances in liquid-phase chemical hydrogen storage, Energy Storage Mater. 26 (2020) 290–312.

[16] Y.P. Qiu, L.L. Zhou, Q. Shi, P. Wang, Free-standing Pt–Ni nanowires catalyst for H$_2$ generation from hydrous hydrazine, Chem. Commun. 57 (2021) 623–626.

[17] K. Wang, Q.L. Yao, S.J. Qing, Z.H. Lu, La(OH)$_3$ nanosheet-supported CoPt nanoparticles: A highly efficient and magnetically recyclable catalyst for hydrogen production from hydrazine in aqueous solution, J. Mater. Chem. A 7 (2019) 9903–9911.

[18] C. Wan, L. Sun, L.X. Xu, D.G. Cheng, F.Q. Chen, X.L. Zhan, Y.R. Yang, Novel NiPt alloy nanoparticle decorated 2D layered g-C$_3$N$_4$ nanosheets: A highly efficient catalyst for hydrogen generation from hydrous hydrazine, J. Mater. Chem. A 7 (2019) 8798–8804.

[19] P. Saha, S. Amanullah, A. Dey, Electrocatalytic reduction of nitrogen to hydrazine using a trinuclear nickel complex, J. Am. Chem. Soc. 142 (2020) 17312–17317.

[20] P.J. Hill, L.R. Doyle, A.D. Crawford, W.K. Myers, A.E. Ashley, Selective catalytic reduction of N$_2$ to N$_2$H$_4$ by a simple Fe complex, J. Am. Chem. Soc. 138 (2016) 13521–13524.

[21] D. Bhattacharjee, S. Dasgupta, Trimetallic NiFePd nanoalloy catalysed hydrogen generation from alkaline hydrous hydrazine and sodium borohydride at room temperature, J. Mater. Chem. A 3 (2015) 24371–24378.

[22] Q.L. Yao, K. Yang, W. Nie, Y. Li, Z.H. Lu, Highly efficient hydrogen generation from hydrazine borane via a MoO$_x$-promoted NiPd nanocatalyst, Renew. Energy 147 (2020) 2024–2031.

[23] S.K. Singh, A.K. Singh, K. Aranishi, Q. Xu, Noble-metal-free bimetallic nanoparticle-catalyzed selective hydrogen generation from hydrous hydrazine for chemical hydrogen storage, J. Am. Chem. Soc. 133 (2011) 19638–19641.

[24] X.Y. Liu, Y. Liu, J.C. Wang, J.H. Ma, Anatase-type TiO$_2$-modified amorphous NiMo nanoparticles with superior catalytic performance toward dehydrogenation of hydrous hydrazine, Ind. Eng. Chem. Res. 61 (2022) 1636–1643.

[25] W. Gao, C. Li, H. Chen, M. Wu, S. He, M. Wei, D. Evans, X. Duan, Supported nickel-iron nanocomposites as a bifunctional catalyst towards hydrogen generation from N$_2$H$_4$·H$_2$O, Green. Chem. 16 (2014) 1560–1568.

[26] K.V. Manukyan, A. Cross, S. Rouvimov, J. Miller, A.S. Mukasyan, E.E. Wolf, Low temperature decomposition of hydrous hydrazine over FeNi/Cu nanoparticles, Appl. Catal. A 476 (2014) 47–53.

[27] J.J. Zhang, K. Kang, Z.Q. Yang, H.B. Dai, D.W. Zhuang, P. Wang, A cost-effective NiMoB–La(OH)$_3$ catalyst for hydrogen generation from decomposition of alkaline hydrous hydrazine solution, J. Mater. Chem. A 1 (2013) 11623–11628.

[28] J. Wang, Y. Li, Y. Zhang, Precious-metal-free nanocatalysts for highly efficient hydrogen production from hydrous hydrazine, Adv. Funct. Mater. 24 (2014) 7073–7077.

[29] Y. Liu, X.Y. Liu, X.Y. Liu, Y.J. Li, J.H. Ma, C. Ma, TiO$_2$ nanoparticle-supported Ni catalyst for the dehydrogenation of hydrazine hydrate, Chemosphere 313 (2023), 137608.

[30] Y.P. Qiu, Q. Shi, L.L. Zhou, M.H. Chen, C. Chen, P.P. Tang, G.S. Walker, P. Wang, NiPt nanoparticles anchored onto hierarchical nanoporous N-doped carbon as an efficient catalyst for hydrogen generation from hydrazine monohydrate, ACS Appl. Mater. Interfaces 12 (2020) 18617–18624.

[31] Y.Y. Ding, W.F. Peng, L. Zhang, J.H. Xia, G. Feng, Z.H. Lu, Chromic hydroxide-decorated palladium nanoparticles confined by amine-functionalized mesoporous silica for rapid dehydrogenation of formic acid, J. Colloid Interface Sci. 630 (2023) 879–887.

[32] P.P. Zhao, N. Cao, W. Luo, G.Z. Cheng, Nanoscale MIL-101 supported RhNi nanoparticles: An efficient catalyst for hydrogen generation from hydrous hydrazine, J. Mater. Chem. A 3 (2015) 12468–12475.

[33] S.K. Singh, Q. Xu, Bimetallic nickel-iridium nanocatalysts for hydrogen generation by decomposition of hydrous hydrazine, Chem. Commun. 46 (2010) 6545–6547.

[34] L. He, Y.Q. Huang, X.Y. Liu, L. Li, A.Q. Wang, X.D. Wang, C.Y. Mou, T. Zhang, Structural and catalytic properties of supported Ni-Ir alloy catalysts for H$_2$ generation via hydrous hydrazine decomposition, Appl. Catal. B Environ. 147 (2014) 779–788.

[35] H.L. Wang, J.M. Yan, Z.L. Wang, S.I. O, Q. Jiang, Highly efficient hydrogen generation from hydrous hydrazine over amorphous Ni$_{0.9}$Pt$_{0.1}$/Ce$_2$O$_3$ nanocatalyst at room temperature, J. Mater. Chem. A 1 (2013) 14957–14962.

[36] H.L. Wang, J.M. Yan, S.J. Li, X.W. Zhang, Q. Jiang, Noble-metal-free NiFeMo nanocatalyst for hydrogen generation from the decomposition of hydrous hydrazine, J. Mater. Chem. A 3 (2015) 121–124.

[37] D.D. Wu, M. Wen, C. Gu, Q.S. Wu, 2D NiFe/CeO$_2$ basic-site-enhanced catalyst via in-situ topotactic reduction for selectively catalyzing the H$_2$ generation from N$_2$H$_4$·H$_2$O, ACS Appl. Mater. Interfaces 9 (2017) 16103–16108.

[38] H. Yen, Y. Seo, S. Kaliaguine, F. Kleitz, Role of metal-support interactions, particle size, and metal-metal synergy in CuNi nanocatalysts for H$_2$ generation, ACS Catal. 5 (2015) 5505–5511.

[39] X.L. Hong, Q.L. Yao, J.J. Long, X.G. Li, X.S. Chen, Z.H. Lu, CuNi/La$_2$O$_2$CO$_3$/rGO nanocomposites: An efficient noble-metal-free catalyst for hydrogen evolution from N$_2$H$_4$·H$_2$O, Ind. Eng. Chem. Res. 60 (2021) 16224–16232.

[40] W. Kang, H. Guo, A. Varma, Noble-metal-free NiCu/CeO$_2$ catalysts for H$_2$ generation from hydrous hydrazine, Appl. Catal. B Environ. 249 (2019) 54–62.

[41] H. Yen, Y. Seo, S. Kaliaguine, F. Kleitz, Role of metal-support interactions, particle size, and metal-metal synergy in CuNi nanocatalysts for H$_2$ generation, ACS Catal. 5 (2015) 5505–5511.

[42] M. Shirotori, S. Nishimura, K. Ebitani, Genesis of a bi-functional acid-base site on a Cr-supported layered double hydroxide catalyst surface for one-pot synthesis of furfurals from xylose with a solid acid catalyst, Catal. Sci. Technol. 6 (2016) 8200–8211.

[43] D. Wu, M. Wen, X. Lin, Q. Wu, C. Gu, H. Chen, A NiCo/NiO-CoO$_x$ ultrathin layered catalyst with strong basic sites for high-performance H$_2$ generation from hydrazine, J. Mater. Chem. A 4 (2016) 6595–6602.

[44] Y.L. Wang, J.W. Wan, J. Ding, J.S. Hu, D. Wang, A rutile TiO$_2$ electron transport layer for the enhancement of charge collection for efficient perovskite solar cells, Angew. Chem. Int. Ed. 58 (2019) 9414–9418.

[45] R. Wang, M.S. Shi, F.Y. Xu, Y. Qiu, P. Zhang, K.L. Shen, Q. Zhao, J.G. Yu, Y. F. Zhang, Graphdiyne-modified TiO$_2$ nanofibers with osteoinductive and enhanced photocatalytic antibacterial activities to prevent implant infection, Nat. Commun. 11 (2020) 4465.

[46] Q.B. Xia, Z.H. Lin, W.H. Lai, Y.F. Wang, C. Ma, Z.C. Yan, Q.F. Gu, W.F. Wei, J. Z. Wang, Z.Q. Zhang, H.K. Liu, S.X. Dou, S.L. Chou, 2D titania–carbon superlattices vertically encapsulated in 3D hollow carbon nanospheres embedded with 0D TiO$_2$ quantum dots for exceptional sodium-ion storage, Angew. Chem. Int. Ed. 58 (2019) 14125–14128.

[47] T.B. Song, H. Chen, Z. Li, Q.J. Xu, H.M. Liu, Y.G. Wang, Y.Y. Xia, Creating an air-stable sulfur-doped black phosphorus-TiO$_2$ composite as high-performance anode material for sodium-ion storage, Adv. Funct. Mater. 29 (2019) 1900535.

[48] J.M. Yu, S.S. Seo, Y.G. Luo, Y. Sun, S. Oh, C.T.K. Nguyen, C.W. Seo, J.H. Kim, J. Kim, H. Lee, Efficient and stable solar hydrogen generation of hydrophilic rhenium-disulfide-based photocatalysts via chemically controlled charge transfer paths, ACS Nano 14 (2020) 1715–1726.

[49] K. Lan, Y. Liu, W. Zhang, Y. Liu, A. Elzatahry, R.C. Wang, Y.Y. Xia, D. Al-Dhayan, N.F. Zheng, D.Y. Zhao, Uniform ordered two-dimensional mesoporous TiO$_2$ nanosheets from hydrothermal-induced solvent-confined monomicelle assembly, J. Am. Chem. Soc. 140 (2018) 4135–4143.

[50] J.H. Ma, X.Y. Xiao, Y.D. Zou, Y. Ren, X.R. Zhou, X.Y. Yang, X.W. Cheng, Y.H. Deng, A general and straightforward route to noble metal-decorated mesoporous transition-metal oxides with enhanced gas sensing performance, Small 15 (2019) 1904240.

[51] L.L. Duan, C. Hung, J.X. Wang, C.Y. Wang, B. Ma, W. Zhang, Y.Z. Ma, Z.W. Zhao, C. C. Yang, T.C. Zhao, L. Peng, D. Liu, D.Y. Zhao, W. Li, Synthesis of fully exposed single-atom-layer metal clusters on 2D ordered mesoporous TiO$_2$ nanosheets, Angew. Chem. Int. Ed. 61 (2022) e202211307.

[52] Q.Q. Cheng, C.G. Hu, G.L. Wang, Z.Q. Zou, H. Yang, L.M. Dai, Carbon-defect-driven electroless deposition of Pt atomic clusters for highly efficient hydrogen evolution, J. Am. Chem. Soc. 142 (2020) 5594–5601.

[53] E. Lee, C. Park, D.W. Lee, G. Lee, H.Y. Park, J.H. Jang, H.J. Kim, Y.E. Sung, Y. Tak, S.J. Yoo, Tunable synthesis of N,C-codoped Ti^{3+}-enriched titanium oxide support for highly durable PEMFC cathode, ACS Catal. 10 (2020) 12080–12090.

[54] W. Song, H.Q. Zhao, J.Q. Ye, M.M. Kang, S.Y. Miao, Z. Li, Pseudocapacitive Na$^+$ insertion in Ti−O−C channels of TiO$_2$−C nanofibers with high rate and ultrastable performance, ACS Appl. Mater. Interfaces 11 (2019) 17416–17424.

[55] R.N. Yang, S.M. Peng, B. Lan, M. Sun, Z.H. Zou, C.Y. Sun, Z.H. Gao, G.C. Xing, L. Yu, Oxygen defect engineering of β-MnO$_2$ catalysts via phase transformation for selective catalytic reduction of NO, Small 17 (2021) 2102408.

[56] X.Y. Song, D. He, W.Q. Li, Z.J. Ke, J.C. Liu, C.Y. Tang, L. Cheng, C.Z. Jiang, Z. Y. Wang, X.H. Xiao, Anionic dopant delocalization through p-band modulation to endow metal oxides with enhanced visible-light photoactivity, Angew. Chem. Int. Ed. 58 (2019) 16660–16667.

[57] S. Sidhik, J. Velusamy, E.L. Rosa, S.A. Perez-García, G. Ramos-Ortiz, T.L. Luke, Role of carbon nanodots in defect passivation and photo-sensitization of mesoscopic-TiO$_2$ for perovskite solar cells, Carbon 146 (2019) 388–398.

[58] Y.Y. Wang, Y.X. Wang, W.P. Kang, D.W. Cao, C.X. Li, D.X. Cao, Z.X. Kang, D.F. Sun, R.M. Wang, Y.L. Cao, TiO$_2$-coated interlayer-expanded MoSe$_2$/phosphorus-doped carbon nanospheres for ultrafast and ultralong cycling sodium storage, Adv. Sci. 6 (2019), 180122.

[59] X.B. Li, J. Xiong, Y. Xu, Z.J. Feng, J.T. Huang, Defect-assisted surface modification enhances the visible light photocatalytic performance of g-C$_3$N$_4$@C-TiO$_2$ direct Z-scheme heterojunctions, Chin. J. Catal. 40 (2019) 424–433.

[60] Q.Q. Hu, Y.F. Liu, W.A. Li, Y.Q. Wang, W.H. Liao, H.X. Zou, J.R. Li, X.Y. Huang, Enhanced photocatalytic hydrogen evolution under visible-light using C, N co-doped mesoporous TiO$_2$ nanocrystals templated by ionic liquids, Chem. Eng. J. 451 (2023), 138670.

[61] P.P. Qiu, W. Li, K. Kang, B. Park, W. Luo, D.Y. Zhao, J. Khim, Ordered mesoporous C/TiO$_2$ composites as advanced sonocatalysts, J. Mater. Chem. A 2 (2014) 16452.

[62] H. Zou, F. Guo, M. Luo, Q.L. Yao, Z.H. Lu, La(OH)$_3$-decorated NiFe nanoparticles as efficient catalyst for hydrogen evolution from hydrous hydrazine and hydrazine borane, Int. J. Hydrog. Energy 45 (2020) 11641–11650.

[63] Y. Lu, H. Zhang, H. Wang, N. Ma, T. Sun, B.S. Cui, Humic acid mediated toxicity of faceted TiO$_2$ nanocrystals to daphnia magna, J. Hazard. Mater. 416 (2021), 126112.

[64] B.W. He, Z.L. Wang, P. Xiao, T. Chen, J.G. Yu, L.Y. Zhang, Cooperative coupling of H$_2$O$_2$ production and organic synthesis over a floatable polystyrene-sphere-supported TiO$_2$/Bi$_2$O$_3$ S-scheme photocatalyst, Adv. Mater. 34 (2022) 2203225.

[65] Z.Z. Wei, Z.J. Zhao, J. Wang, Q. Zhou, C.X. Zhao, Z.H. Yao, J.G. Wang, Oxygen-deficient TiO$_2$ and carbon coupling synergistically boost the activity of Ru nanoparticles for the alkaline hydrogen evolution reaction, J. Mater. Chem. A 9 (2021) 10160–10168.

[66] U. Nwankwo, R. Bucher, A.B.C. Ekwealor, M. Maaza, F.I. Ezem, Synthesis and characterizations of rutile-TiO$_2$ nanoparticles derived from chitin for potential photocatalytic applications, Vacuum 161 (2019) 49–54.

[67] K. Yang, K.K. Yang, S.L. Zhang, Y. Luo, Q.L. Yao, Z.H. Lu, Complete dehydrogenation of hydrazine borane and hydrazine catalyzed by MIL-101 supported NiFePd nanoparticles, J. Alloy Compd. 732 (2018) 363–371.

[68] W.J. Zhang, P. Li, H.B. Xu, R.D. Sun, P.H. Qing, Y. Zhang, Thermal decomposition of ammonium perchlorate in the presence of Al(OH)$_3$·Cr(OH)$_3$ nanoparticles, J. Hazard. Mater. 268 (2014) 273–280.

[69] Z.J. Zhang, Z.H. Lu, H.L. Tan, X.S. Chen, Q.L. Yao, CeO$_x$-modified RhNi nanoparticles grown on rGO as highly efficient catalysts for complete hydrogen generation from hydrazine borane and hydrazine, J. Mater. Chem. A 3 (2015) 23520–23529.

[70] C.D. Valentin, G. Pacchioni, A. Selloni, Theory of carbon doping of titanium dioxide, Chem. Mater. 17 (2005) 6656–6665.

[71] K. Lau, F. Niemann, K. Abdiaziz, M. Heidelmann, Y.K. Yang, Y.J. Tong, M. Fechtelkord, T.C. Schmidt, A. Schnegg, R.K. Campen, B.X. Peng, M. Muhler, S. Reichenberger, S. Barcikowski, Differentiating between acidic and basic surface hydroxyls on metal oxides by fluoride substitution: A case study on blue TiO$_2$ from laser defect engineering, Angew. Chem. Int. Ed. 62 (2023), e202213968.

[72] C. Hu, Y. Zhang, Y. Zhou, Z.F. Liu, X.S. Feng, Unsymmetrical dimethylhydrazine and related compounds in the environment: Recent updates on pretreatment, analysis, and removal techniques, J. Hazard. Mater. 432 (2022), 128708.

[73] F. Sun, J.S. Qin, Z.Y. Wang, M.Z. Yu, X.H. Wu, X.M. Sun, J.S. Qiu, Energy-saving hydrogen production by chlorine-free hybrid seawater splitting coupling hydrazine degradation, Nat. Commun. 12 (2021) 4182.